Clays and Clay Minerals, Vol. 58, No. 5, 667–681, 2010.

EFFECT OF A THERMAL GRADIENT ON IRON-CLAY INTERACTIONS

Marie-Camille Jodin-Caumon[1,*], Regine Mosser-Ruck[1], Davy Rousset[1], Aurelien Randi[1], Michel Cathelineau[1], and Nicolas Michau[2]

[1] G2R, Nancy-Université, CNRS, BP 70239, 54506 Vandœuvre-lès-Nancy, France
[2] Agence Nationale pour la Gestion des Déchets Radioactifs (ANDRA), Direction Scientifique/Service Colis et Matériaux, Parc de la Croix Blanche, 1/7 rue Jean Monnet, 92298 Châtenay-Malabry Cedex, France

Abstract—Disposal facilities in deep geological formations are considered to be a possible solution for long-term management of high-level nuclear waste (HLW). The design of the repository generally consists of a multiple-barrier system including Fe-based canisters and a clay backfill material. The Fe-clay system will undergo a thermal gradient in time and space, the heat source being the HLW inside the canisters. In the present paper, the effect of a thermal gradient in space on Fe-smectite interactions was investigated. For this purpose, a tube-in-tube experimental device was developed and an 80−300ºC thermal gradient was applied to a mixture of MX80 bentonite, metallic Fe (powder and plate), magnetite, and fluid over periods of 1 to 10 months. Transformed and newly formed clay minerals were characterized by scanning electron microscopy, transmission electron microscopy, X-ray diffraction, and Mössbauer spectroscopy. The main mineralogical transformations were similar to those described for batch experiments: smectite was destabilized into an Fe-enriched trioctahedral smectite and Fe-serpentine or chlorite as a function of the experimental conditions. Newly formed clay was observed all along the walls of the gold tube. Their crystal chemistry was clearly different from the clays observed in the hot and cold part of the tubes. The thermal diffusion of elements was also observed, especially that of Mg, which migrated toward the hottest parts of the tubes. In the end, the thermal gradient affected the redox equilibria; more reduced conditions were observed in the hotter parts of the tubes.

Key Words—Bentonite, Iron, MX80, Smectite, TEM-EDS, Thermal Gradient.

INTRODUCTION

Repositories created in deep geological formations are believed by many to be the solution for the disposal of long-term HLW. One of the designs consists of a multiple-barrier system comprising vitrified waste placed inside a steel canister surrounded by backfill material and deposited into host rock. Bentonite is a possible backfill material. It was chosen because of its adsorption, swelling, self sealing, thermal and hydraulic conductivity, and long-term stability properties (*e.g.* Madsen, 1998; Trouiller, 2006). The bentonite material may, however, be affected by heat and radiation emissions by HLW, corrosion of the canister, and desaturation/resaturation processes. In this context, the present study was undertaken to investigate the possible mineralogical evolution of clays in contact with metallic Fe under various conditions simulating those of a HLW repository. Despite large variability in the experimental or modeling conditions (nature of the clay material, fluid, Fe supply, fluid/rock ratio, temperature, pH, redox conditions, duration, *etc.*), smectite in the presence of Fe generally may be converted into an Fe-rich di- or trioctahedral smectite, such as Fe-saponite, 1:1 Fe-phyllosilicate (berthierine, cronstedtite, odinite, greenalite), or even Fe-chlorite (chamosite) at elevated temperatures. The simultaneous formation of magnetite, quartz, zeolite, and siderite has also been reported as a function of Fe content, redox conditions, temperature, and pCO_2 (*e.g.* Guillaume *et al.*, 2003; Neaman *et al.*, 2003; Lantenois *et al.*, 2005; Bildstein *et al.*, 2006; Charpentier *et al.*, 2006; Wilson *et al.*, 2006a, 2006b; Carlson *et al.*, 2007; de Combarieu *et al.*, 2007; Perronnet *et al.*, 2007; Martin *et al.*, 2008; Perronnet *et al.*, 2008; Schlegel *et al.*, 2008; Savage *et al.*, 2010).

Most of the experimental studies were performed in batch mode at a constant and uniform temperature. The HLW repository design, however, generates a thermal gradient in space (from the wastes to the host rock) and in time (progressive decrease in the temperature of the HLW with decreasing radioactivity). A thermal gradient may imply that mass transport phenomena are occurring by convection and diffusion processes. In addition to ordinary diffusive transport, thermal diffusion is a molecular phenomenon which may create a concentration gradient (the Soret effect: Chipman, 1926) and is a function of temperature, temperature gradient, and the nature of the chemical elements (*e.g.* Rosanne *et al.*, 2003). The effect of a thermal gradient on clay products in conditions close to those of a HLW repository have been studied. Vidal and co-workers (Vidal, 1997; Vidal and Durin, 1999; Baldeyrou *et al.*, 2003) carried out

* E-mail address of corresponding author:
Marie-Camille.Caumon@g2r.uhp-nancy.fr
DOI: 10.1346/CCMN.2010.0580506

tube-in-tube experiments which revealed that local equilibria at each point of the tube may evolve with time in relation to nearby local equilibria. Poinssot *et al.* (1996, 1997, 1998) demonstrated that mass transport under a thermal gradient affected the chemical elements differently in their experiments: the lightest elements such as Si, Al, and Na were preferentially found in the cooler part whereas the heavier elements Fe and Ca were concentrated in the hotter part. This partitioning appeared to be independent of the absolute temperature. As a consequence, the chemical composition of the different regions depended on the thermal gradient whereas the crystallinity of secondary phases depended on the absolute temperature. Martín *et al.* (2000) calculated thermal diffusion coefficients of various ions in a complex mixture. They demonstrated the greater mobility of Cl^-, Na^+, and Ca^{2+} and the dependency of the apparent diffusion coefficient on the experimental conditions: in their experiments, the mobility of Na^+ appeared to be less because it was constrained by the equilibrium of ionic charges. Rosanne *et al.* (2003, 2006) and Paszkuta *et al.* (2006) demonstrated that mass transfer through a compacted clayey sample could be enhanced by the Soret effect, and that the computed Soret coefficients for Na^+ and Cl^- were five times greater than in the corresponding free fluid. Those authors attributed this to the coupling of diffusion phenomena with electrical phenomena at the pore scale. Finally, quantifying or predicting the intensity of thermal diffusion in real systems is difficult compared to convection or normal diffusive transport phenomena because it depends heavily on the experimental design and conditions (temperature, thermal gradient, concentrations, nature of the electrolyte, geometry of the reactor, *etc.*).

The aim of this study was to describe smectite transformations in contact with metallic Fe along a continuous thermal gradient. An experimental design simulating a thermal gradient in a HLW repository was developed. Mineralogical transformations were characterized using Transmission Electron Microscopy (TEM), Scanning Electron Microscopy (SEM), X-ray diffraction (XRD), and Transmission Mössbauer Spectroscopy (TMS). The results were compared qualitatively to those from standard batch experiments in order to evaluate the extent of the effect of thermal diffusion on reaction pathways and rates.

MATERIALS AND METHODS

Reactants

The clay used was MX80 bentonite (Na/Ca-bentonite from Wyoming, USA) consisting of montmorillonite (79%), plagioclases (9%), quartz (3%), mica (3%), K-feldspars (2%), carbonates (2%), and other minerals (2%, mostly pyrite, phosphates, and hematite). The structural formula of the montmorillonite: $Na_{0.16}Ca_{0.09}(Si_{3.97}Al_{0.03})(Al_{1.59}Mg_{0.22}Fe(III)_{0.10}Fe(II)_{0.09})O_{10}(OH)_2$ was determined by TEM-EDS and TMS analyses (Sauzéat *et al.*, 2001; Guillaume, 2002; Guillaume *et al.*, 2003). The $Fe(III)/Fe_{total}$ ratio (0.55), unusual in a montmorillonite, is close to the data of Carlson *et al.* (2007) who published an $Fe(III)/Fe_{tot}$ ratio of 0.64.

Starting mixtures consisted of magnetite, metallic Fe powder (Riedel-de-Haën, >99.5%), and MX80 bentonite, reacting with either Milli-Q water (18.2 MΩ-cm) or a low-salinity NaCl-$CaCl_2$ aqueous solution (0.0207 mol kg^{-1} NaCl and 0.0038 mol kg^{-1} $CaCl_2$) (Table 1). The liquid to clay mass ratio (L/C) was fixed at 10. The Fe to clay mass ratio (I/C) was set to 0.1, with a 50/50 w/w mix of magnetite and metallic Fe (except experiment 1m in which Fe was present as metallic Fe only). The experimental conditions were similar to those of Guillaume *et al.* (2002, 2003, 2004).

Tube-in-tube experiments

The experimental design (Figure 1) was derived from those used in previous works (Goffé *et al.*, 1987; Robert and Goffé, 1993; Vidal, 1997; Poinssot *et al.*, 1998; Baldeyrou *et al.*, 2003; Rousset *et al.*, 2006). The powder mixture (clay, metallic Fe, and magnetite, except experiment 1m that only contained MX80 and metallic

Table 1. Experimental conditions and mean temperature in each section (precipitation niches).

Experiment	Fluid	Duration (months)	Temperature (ºC)						
			Section 1	Section 2	Section 3	Section 4	Section 5	Section 6	Section 7
1m	H_2O	1	**300**	260	225	190	155	125	**80**
3m-ip300	NaCl-$CaCl_2$	3	**300**	250	215	185	150	115	**80**
3m-ip80	NaCl-$CaCl_2$	3	**300**	260	225	190	155	125	**80**
6m-ip300	H_2O	6	**300**	260	220	185	145	**100**	–
6m-ip100	H_2O	6	**300**	255	220	180	145	**100**	–
10m-ip300	NaCl-$CaCl_2$	10	**300**	255	225	190	160	125	**80**
10m-ip80	NaCl-$CaCl_2$	10	**300**	260	225	190	160	125	**80**

Bold: sections containing platinum capsules.
The numbers 300, 100, or 80 in the names of the experiments indicate the position of the iron plate (ip) in the hot (300ºC) or cold (100 or 80ºC) part of the tube.

https://doi.org/10.1346/CCMN.2010.0580506 Published online by Cambridge University Press

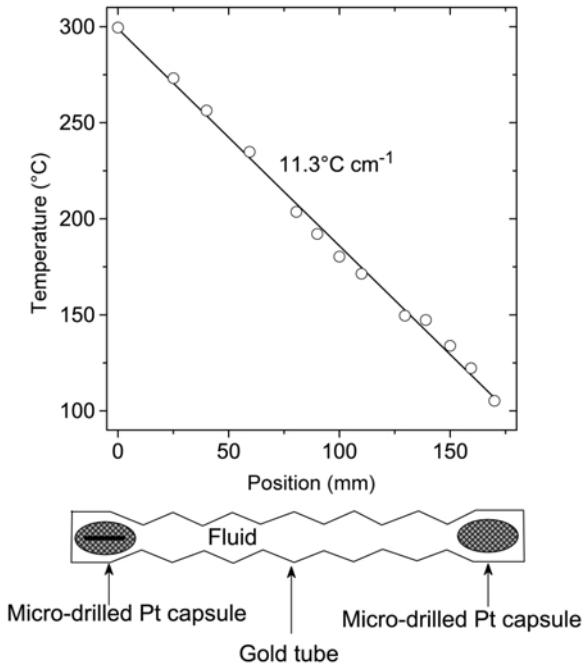

Figure 1. Thermal gradient of experiment 10m-ip80 and schematic drawing of the tube-in-tube experiments. Both Pt capsules contain bentonite, Fe, and magnetite powders. One of the capsules contained an Fe plate.

Fe) was loaded into two 3 cm long Pt capsules (diameter 4 mm). An Fe plate (15 or 30 mg) was added to the mixture in one of the two Pt capsules, except in experiment 1m. The capsules had previously been drilled (∅ 200 μm) to favor the migration of the fluid and of individual particles or small aggregates along the tube. The holes were thought to be small enough to limit the migration of large clay aggregates. The two Pt capsules were then closed by pinching their extremities and putting them inside each end of a 20 cm long Au tube filled with a fluid (H_2O or a NaCl-$CaCl_2$ solution). The loading of the Au tube was achieved in a glove box under argon to limit the amount of O_2 in the reactor. The Au tube was welded and regularly pinched to form six or seven precipitation niches ~3 cm long. An 80−300ºC (or 100−300ºC) thermal gradient was applied to the tube by placing it in an autoclave, with one extremity in an oven and the other in a bomb cooled by circulating cold water. Parallel experiments were carried out with the Fe plate located either in the hot or the cold part, to check the reversibility of the reactions.

The thermal gradient was constant during the experiments and fixed by the temperature of the oven, the flow of the cold water in the bomb, the length of the Au tube, and the relative position of the autoclave between the oven and the cold bomb. Temperature was controlled to ±1ºC throughout the experiments by monitoring it with two thermocouples placed inside the autoclave at each end of the Au tube. The thermal gradient was calibrated before each experiment (see example in Figure 1). A stable, quasi-linear thermal gradient at ~12.0±0.1ºC cm^{-1} was obtained, so that the intermediary niches (section 2 to 5 or 6) corresponded to a range of temperature of 30−40ºC and the end sections to a range of temperature of 45−55ºC (Table 1). At the end of the experiments (1−10 months, Table 1), the autoclave was cooled quickly with water (a few minutes were required to reach ambient temperature). The Au tube was carefully kept horizontal while being quenched in liquid N_2 to freeze the liquid phase and avoid any particle movement after the experiment. The Au tube was then cut into six or seven sections corresponding to the precipitation niches and kept in a freezer until analyzed. Sections 1 and 6 (or 7), corresponding to the hot and cold part, respectively, each contained a Pt capsule. The labeling of the experiments indicates the duration of the experiment (1, 3, 6, or 10 months) followed by the position of the Fe plate in the Pt capsule in the hot part at 300ºC (ip300) or in the cold part at 100ºC or 80ºC (ip100 or ip80). Each experiment was divided into sections: the corresponding samples were labeled as the mean temperature of the section and Pt or Au in relation to the location of the sample inside a Pt capsule (hot and cold part) or on the Au tube walls (all along the tube, including the hot and cold parts) (Table 1, Figure 1). As an example, the sample 10m-ip300/300Pt corresponds to the particles found inside the Pt capsule in the hot part (300Pt) of the 10 month experiment (10m) with the Fe plate in the hot part (ip300).

Sample analyses

Powder samples from the Pt capsules or on the Au tube walls were analyzed by SEM, TEM imaging, and TEM-EDS. Electron diffraction, XRD, and TMS analyses were performed when enough powder was available.

SEM. Powder samples were dispersed in ethanol. A droplet was deposited on a carbon plate and evaporated in air. The SEM images were obtained using an Hitachi FEG S4800 electron microscope, equipped with a LaB_6 gun under a residual pressure of 10^{-6} mbar. Metal coating was not necessary because the clay particles were sufficiently thin and dispersed to avoid charging.

TEM. The TEM images, electron dispersive spectra, and electron diffraction patterns were obtained on powder samples dispersed in ethanol and deposited on a micro grid (Formvar/Carbon 300 Mesh Ni, Agar Scientific). The Philips CM20 electron microscope operated at 200 kV and was equipped with a Si-Li detector and Li super ultra-thin windows. Microchemical analyses of isolated clay particles were obtained with an EDAX energy dispersive X-ray analyzer attached to the electron microscope. Spectra were collected under nanoprobe mode, over a period of 40 s, from an area ~10 nm in

https://doi.org/10.1346/CCMN.2010.0580506 Published online by Cambridge University Press

diameter. Elemental composition was calculated assuming the thin-film criteria (SMTF program: semi-quantitative metallurgical thin-film program) and using k-factors calibrated with independently analyzed macroscopic micas, with a maximum error of 5% for each element. Twenty to 30 analyses were performed on isolated particles for each sample. The relative proportions of Si, Al, Fe, Mg, Na, Ca, K, Ti, and S were measured in all the samples. K, Ti, and S were checked but only trace levels were found. Structural formulae were calculated on the basis of 22 negative charges per half unit cell, *i.e.* $O_{10}(OH)_2$ basis, and the elemental composition of the clay with respect to each element is reported here in units of atoms per formula unit (a.p.f.u). The tetrahedral sheet was assumed to be filled with $(4-x)$ Si and x Al atoms (denoted ^{IV}Al). The octahedral sheet was composed of Fe, Mg, and the remaining Al (denoted ^{VI}Al). The possible octahedral and tetrahedral charge deficiencies were balanced by the interlayer cations, Na and Ca, and are expressed in equivalents per formula unit or equivalents per half unit cell. With respect to Fe, Guillaume *et al*. (2004) reported the variation of the Fe oxidation state in MX80 in the presence of Fe oxides as a function of temperature between 80ºC and 300ºC. Because the samples in the present study were submitted to a large temperature range (80−300ºC), Fe was arbitrarily assumed to be 100% Fe(III) when no TMS data on Fe oxidation state were available. As a consequence, the results are only discussed comparing the relative variations of the elemental contents and interlayer charge per formula unit (half unit cell). Reference clay minerals (Kostov, 1968; Caillère *et al.*, 1982) were added to some of the diagrams to represent the poles of possible crystal chemical modifications.

XRD. The XRD data were collected from unoriented powder samples on a Zero Background Holder (Silicon holder) using a Philips Xpert Pro diffractometer with non-monochromatic CuKα radiation (λ_1 = 1.54056 Å, λ_2 = 1.54439 Å). The signal of the holder was not subtracted, so the XRD patterns showed a decreased background and a small bump at ~8º2θ.

TMS. The TMS spectra of powders were acquired at a temperature of 78 K by means of a constant-acceleration spectrometer with a 50 mCi source of ^{57}Co in Rh. Adjustments of the spectra were performed using Lorentzian-shape lines (Guillaume *et al.*, 2003).

RESULTS AND DISCUSSION

Morphology of the reaction products (SEM and TEM analyses)

Clay fraction. The morphology of the clayey reaction products in the whole of the samples, as observed in electron micrographs, was similar to the starting montmorillonite, *i.e.* isolated and aggregated flakes, whatever the duration of the experiment or temperature (see examples in Figure 2a,b). The fine structure (Figure 2c) was layered with a mean interlayer spacing of 10−13 Å, a typical value for a smectite with variable water loss

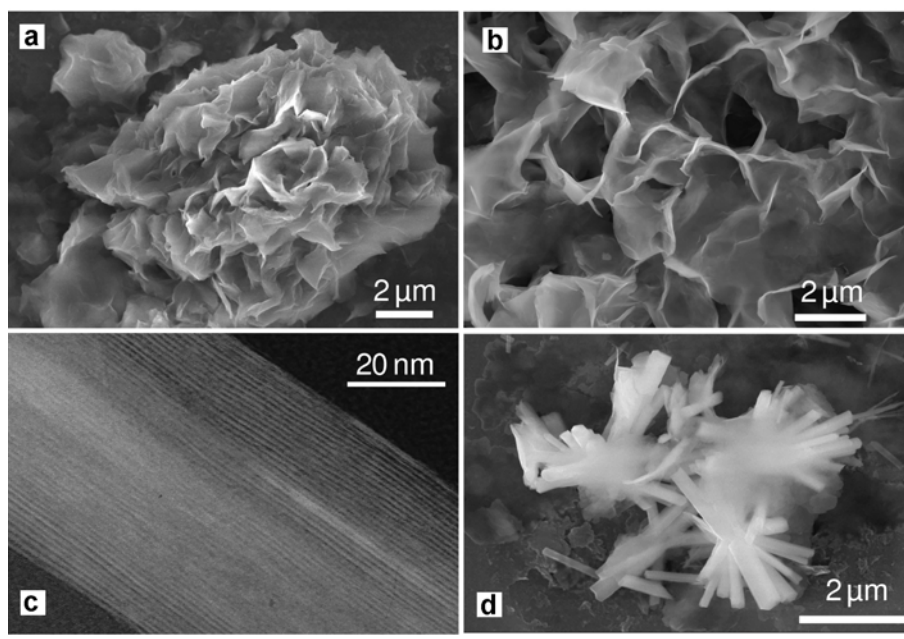

Figure 2. Examples of SEM (a,b,d) and TEM (c) photomicrographs of the clay phase (a,b,c) and of albite (d) at the end of the experiments. (a) 10m-ip80/80Pt; (b) 6mip300/260Au; (c) 6m-ip300/300Au; (d) 10m-ip80/300Pt.

https://doi.org/10.1346/CCMN.2010.0580506 Published online by Cambridge University Press

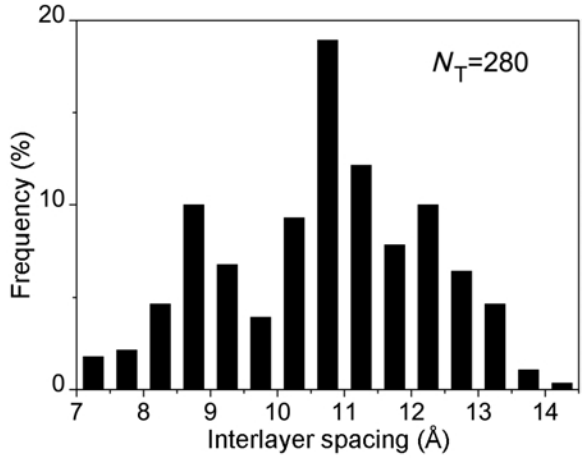

Figure 3. Distribution of interlayer spacings measured from TEM images of sample 10m-ip300/300Pt (Figure 4). The total number of measurements, N_T = 280, corresponds to 1367 measured layers.

under the vacuum of the electron microscope. The interlayer spacings were measured from several TEM images. As the interlayer spacings were too small to be measured accurately one by one, they were measured on micrographs by groups of several layers, the total thickness being divided by the number of layers in the group. The values of 280 measurements on sample 10m-ip300/300Pt are represented in a histogram (Figure 3), which shows that the distribution of the layer sizes was centered around 10.5–11 Å, the normal *d* value for a dehydrated smectite. Some smaller interlayer spacings (7 Å) were found, which alternated with 10–13 Å spacings (Figure 4a) or formed small groups (Figure 4b) to yield a mean value of 8.5–9 Å. A few isolated 14 Å spacings were also found.

Similar observations were reported by Wilson *et al.* (2006a, 2006b) in the case of batch experiments conducted on montmorillonite reacted with Fe over a period of 3.5 months at 250ºC in a 36 mM NaCl solution. The authors reported interlayer spacings in the range 10–13 Å for the unaltered smectite as a function of the collapsing degree of the layers under vacuum. They also reported the presence of 7 Å layers alternating with 10–13 Å spacings. The authors suggested that the areas where 7 Å layers were intercalated were due to a partial dissolution of one of the tetrahedral sheets of the original smectite and may precede the formation of berthierine or chlorite-like phases. On the contrary, no intercalated layers were observed in the range 11–14 Å, so the largest values may correspond to hydrated or partially dehydrated smectite and/or to a 14 Å phase such as chlorite.

Other minerals. The other phases observed in SEM images were mainly amorphous and crystalline silica, rod-shaped products (Figure 2d), and a few Fe oxides. Silica resulted either from dissolution/precipitation processes of the clay phase or from siliceous phases initially present in the sample, such as quartz. Silica products were mainly amorphous at the lowest temperature (80ºC). At higher temperature, altered and newly formed quartz were observed. Fe oxides (probably magnetite because of the octahedral shape of the crystals) were only observed in images at 80 or 100ºC for the shortest reaction times. They issued from unreacted magnetite and/or oxidation of the Fe powder and plate. Finally, small fibrous-radiated aggregates were observed in some samples at elevated temperatures ($\geqslant$240ºC). They were more abundant with time, particularly in samples 6m-ip300/300Pt, 10m-ip300/300Pt, and 10m-ip80/300Pt. Albite

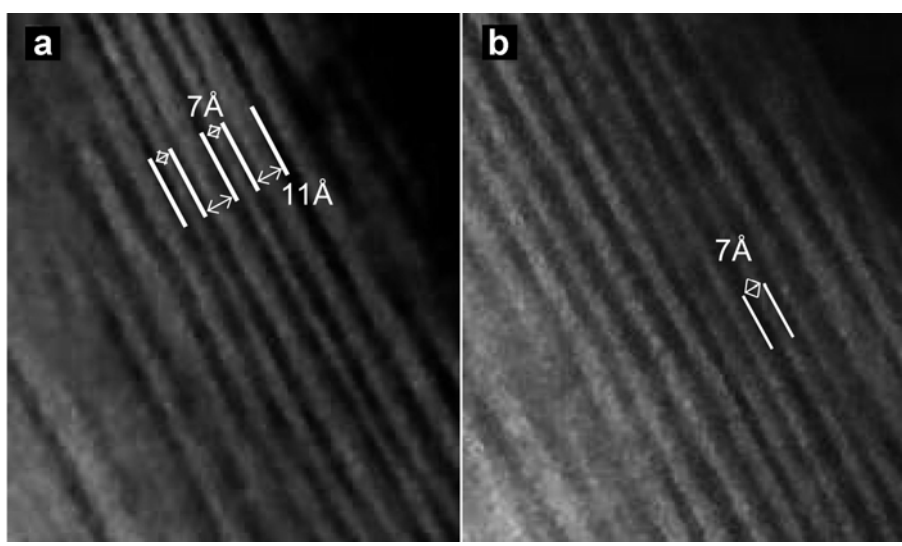

Figure 4. TEM images of the clay particles in sample 10m-ip300/300Pt. Small interlayer spacings (7 Å) alternate with 10–13 Å spacings (a) or form small groups (b).

https://doi.org/10.1346/CCMN.2010.0580506 Published online by Cambridge University Press

was identified by XRD and TEM (chemical analysis and electron diffraction).

Crystal chemistry of the clay minerals inside the platinum capsules

In the hot parts. At 300ºC (Figure 5), the crystal chemistry of the clay particles inside the Pt capsules was heterogeneous but some trends appeared. The Si content decreased to 3.2, 2.7, 2.4, and then 2.1 (all elemental compositions are in a.p.f.u. unless noted otherwise) after 1, 3, 6, and 10 months, respectively (Figure 5a), while during the same periods, the Fe and Mg contents increased to 1.4, 1.9, 2.1, and 2.4 and 0.3, 0.6, 1.0, and 0.9, respectively (Figure 5c). The ratio Fe/(Fe + Mg) quickly reached a plateau at 0.8 (Figure 5d). The interlayer charge (I.C.) remained about constant or increased slightly overall, except for the clay particles with the smallest Si contents for which the I.C. became very small (<0.15 − layer charge units are equivalents per formula unit, eq./f.u., unless noted otherwise) (sample 10m-ip80/300Pt, open stars in Figure 5a). The interlayer composition evolved in relation to the interlayer charge. The Ca contents remained about constant or increased slightly. The Na content was equal to or slightly greater than that of the starting smectite in all the samples, except sample 10m-ip80/300Pt in which the Na content was close to zero (Figure 5e). These variations were too weak to be correlated to the parameters of the experiments, including the nature of the fluid. They were probably due to complex phenomena of hydrolysis and cation exchange. The Al content was almost constant (total Al = 1.62, dotted line in Figure 5b) except in samples 6m-ip300/300Pt and 10m-ip80/300Pt in which the total Al contents increased to 2.2 and 2, respectively. The initial chemical composition of the fluid (pure water *vs.* a low-salinity solution) and the position of the Fe plate had no visible effects on the path and kinetics of transformation. Finally, some particles in sample 10m-ip300/300Pt displayed unrealistic negative ^{VI}Al values; the strong decrease of the Si content (down to 2.1-2.3) at a constant Al content (~1.6) resulted in a sum of Al + Si of <4 in the tetrahedral sheet. This group of particles also displayed a very small I.C. value, <0.13, corresponding to a small Ca content, which was still ⩾ the amount of Na, and to very large Fe and Mg contents (2.1−2.4 and 0.6−0.8, respectively). These values are located in the chlorite area and/or Fe-serpentine areas of Figure 5. No difference in habit was observed in the photomicrographs. The structural formulae, calculated on the basis of $O_{10}(OH)_8$ for chlorite instead of $O_{10}(OH)_2$ for smectite, was $Ca_{0.06}(Fe(III)_{2.87}Al_{0.92}Mg_{0.87})(Si_{2.75}Al_{1.25})O_{10}(OH)_8$.

In the cold parts. At 80ºC (or 100ºC), the crystal chemistry was more homogeneous than in the hot parts (Figure 6, note that the scales are different from those in Figure 5). The Si content decreased down to 3.6 after 1 month (empty square), and then reached a minimum at 3.4 (Figure 6a). From 6 months, the I.C. decreased to 0.1 for samples without an Fe plate (open symbols) and to nearly zero for samples with an Fe plate (filled symbols). The decrease in the I.C. was due to the loss of both the Na and Ca cations (Figure 6e). The Al and Mg contents were almost constant or decreased slightly (Figure 6b,c). The Fe content increased to 0.7 after only 1 month and then stabilized at ~1.1, independent of the presence of an Fe plate, resulting in an Fe/(Fe + Mg) ratio of ~0.8 (Figure 6d). The transformations after 6 months (circles in Figure 6) were in some cases more intense than those observed after 10 months (stars in Figure 6), probably because the cold part of the experiments for samples 6m-ip300 and 6m-ip100 was at 100ºC instead of 80ºC (Table 1). No significant effect of the nature of the fluid was observed.

Discussion. A decrease in Si content and an increase in Fe content at almost constant Al content were observed in both the hot and cold parts, with rates of transformation which were twice as intense as in the hot parts. The evolution of the crystal chemistry of the clay particles became more intense with time, but the nature of the fluid, *i.e.* pure water *vs.* a low-salinity NaCl-$CaCl_2$ solution, failed to affect the reaction paths and intensities. As the particles were confined in the Pt capsules, the reactive medium was probably buffered by the clay minerals in the first steps of dissolution and/or cation-exchange processes. The main differences between the clay particles in the hot and cold parts involved the Mg content, the I.C., and the effect of the Fe plate position. The Mg content was constant or slightly smaller in the cold parts but increased in the hot parts. The I.C. decreased in the cold parts for the shortest times (Figure 6a), whereas it was almost constant in the hot parts after 1, 3, and 6 months and only decreased after 10 months (Figure 5a). The I.C. was also affected by the presence of an Fe plate, but only in the cold parts. In the end, the clay particles ranged between the domains of low-charge montmorillonite and Fe-serpentine or chlorite. Siliceous products and albite were the main secondary minerals.

These results agreed well with results from other studies (*e.g.* Guillaume *et al.*, 2003, 2004; Wilson *et al.*, 2006a, 2006b; Savage *et al.*, 2010), except for a number of differences, particularly with the results of Guillaume *et al.* (2003, 2004) which were obtained under the same experimental conditions as in the present study (3 and 9 months, at 300ºC and 80ºC, with similar reactants and the same L/C and I/C ratios). Guillaume and co-workers demonstrated in batch experiments at 300ºC that the presence of an Fe plate in the reactor affects the crystal chemistry, with the greatest effect occurring nearest to the Fe plate. Reaction rates were clearly enhanced in the samples closest to the Fe plate, in particular the decrease in Si content and the increase in Fe content. In the present study, however, the presence of an Fe plate affected the intensity of some clay mineral evolutions at

https://doi.org/10.1346/CCMN.2010.0580506 Published online by Cambridge University Press

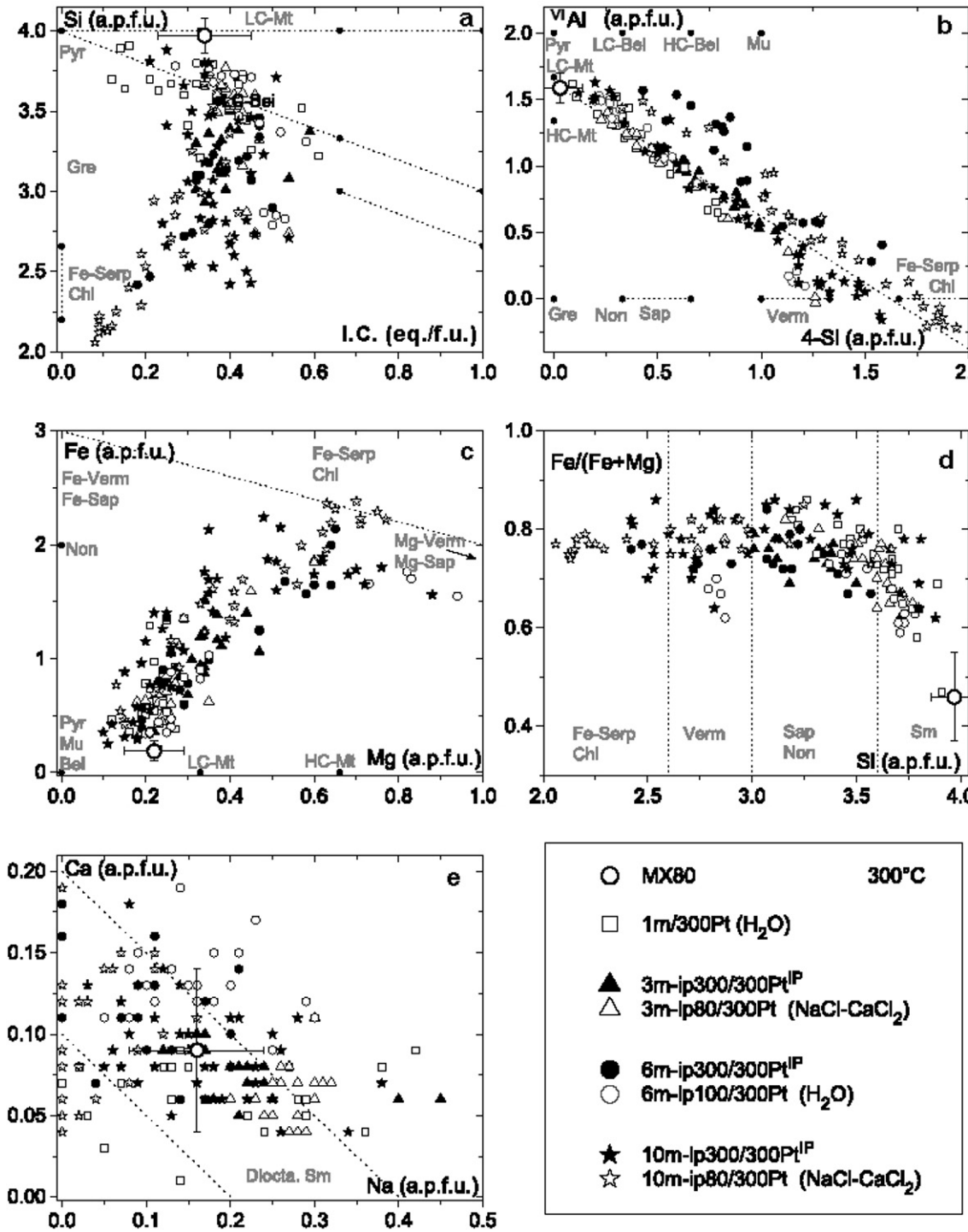

Figure 5. Crystal chemistry (from TEM-EDS) of the clay phase inside the Pt capsules in the hot parts (300ºC) as a function of the position of the Fe plate and duration of the experiments. (a) Si *vs* I.C.; (b) ^{VI}Al *vs.* 4-Si; (c) Fe *vs.* Mg; (d) Fe/(Fe+Mg) *vs.* Si; (e) Ca *vs.* Na. Filled symbols: presence of an Fe plate in the Pt capsule. IP: Fe plate. Reference clays (Kostov, 1968; Caillère *et al.*, 1982): Bei: beidellite; Chl: chlorite; Fe-Serp: Fe-rich 7 Å phases; Gre: greenalite; Mt: montmorillonite; Mu: muscovite; Non: nontronite; Pyr: pyrophyllite; Sap: saponite; Sm: smectite; Verm: vermiculite; LC: low charge; HC: high charge; Al in octahedral sites $^{VI}Al = Al_{Tot} - {}^{IV}Al$ with $^{IV}Al = 4 - Si$; interlayer charge I.C. = Na+K+2Ca. The dotted line in the diagonal of the 4-Si/^{VI}Al diagram indicates a constant total Al content. All structural formulae are calculated on the basis of the half unit cell, *i.e.* $O_{10}(OH)_2$. Other than for Fe/(Fe+Mg), the axis units are atoms per formula unit (a.p.f.u.) or atoms per half unit cell.

https://doi.org/10.1346/CCMN.2010.0580506 Published online by Cambridge University Press

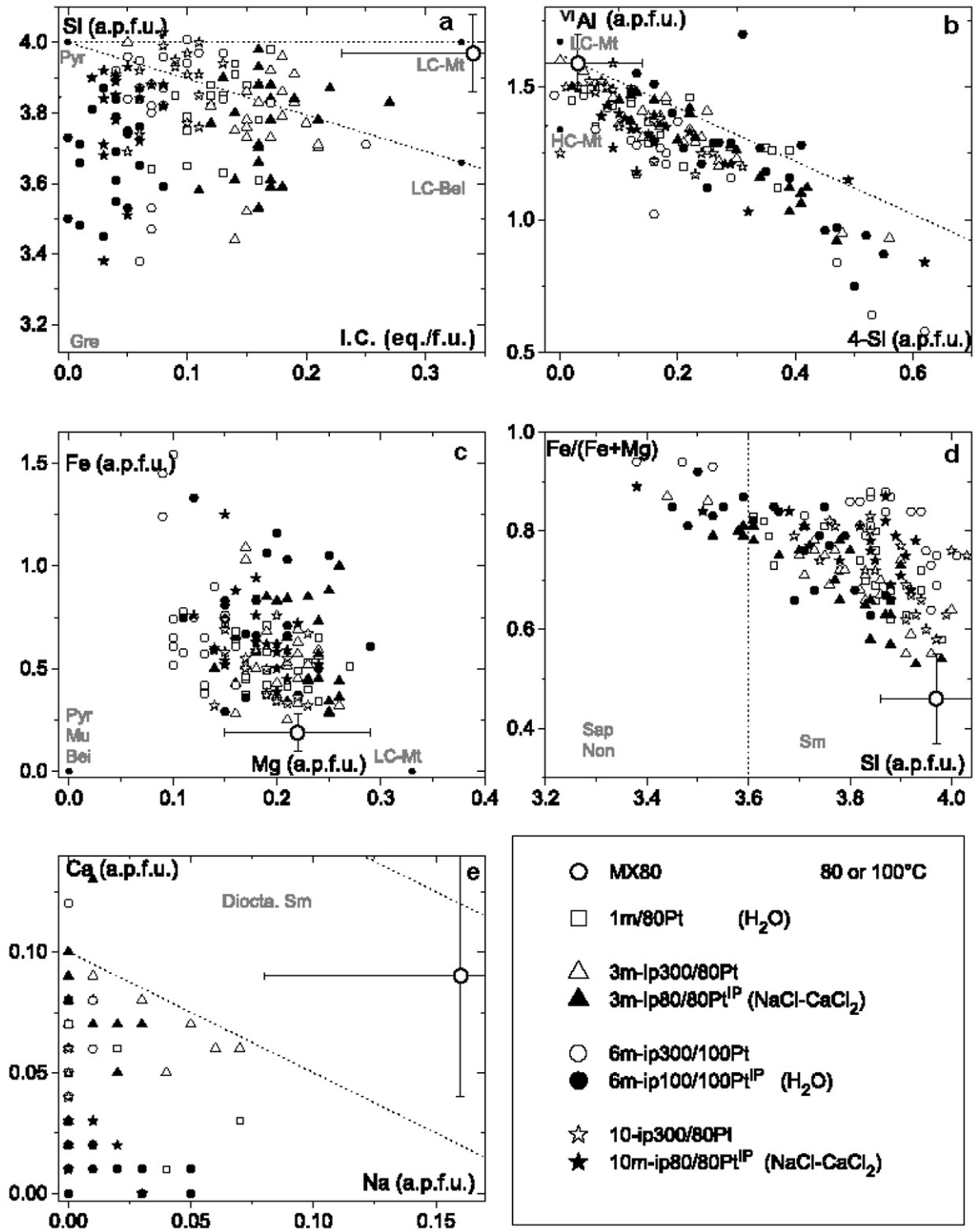

Figure 6. Crystal chemistry (from TEM-EDS) of the clay phase in the Pt capsules in the cold parts (100ºC or 80ºC) as a function of the position of the Fe plate and duration. Filled symbols indicate the presence of an Fe plate in the Pt capsule. IP: iron plate. (a) Si *vs.* I.C.; (b) ^{VI}Al *vs.* 4-Si; (c) Fe *vs.* Mg; (d) Fe/(Fe+Mg) *vs.* Si; (e) Ca *vs.* Na. See Figure 5 for symbol legend and axis units.

https://doi.org/10.1346/CCMN.2010.0580506 Published online by Cambridge University Press

80ºC (or 100ºC) but not at 300ºC, with an effect on the I.C. but not the Fe content. The evolution of the interlayer at 80ºC and 300ºC was the same as in the batch experiments of Guillaume *et al.* (2004), *i.e.* the I.C. was constant regardless of time and temperature. These observations indicated that elemental diffusion occurred between the hot and cold parts of the Au tubes. Considering the precipitation/crystallization of secondary minerals, the balance of cations seems to be equilibrated between the hot and the cold parts. The general loss of Si was balanced by the precipitation of amorphous siliceous products and/or the crystallization of quartz as a function of temperature. Samples 6m-ip300/300Pt and 10m-ip80/300Pt, in which the Al content increased, were the samples for which the greatest amounts of Al-poor albite were found. The increase in Mg (and Ca) in the hot parts might be partially balanced by the losses in the cold parts. The balance of the whole of the elements might be completed by the precipitation of newly formed clays on the Au tube walls between the cold and hot parts and the presence of dissolved species in the fluid. The particles on the Au tube walls were analyzed (see next paragraphs) but not the fluid because the available volumes were too small.

Crystal chemistry of the clay particles on the gold tube walls

The particles found in the precipitation niches resulted either from dissolution/precipitation processes or from particles which escaped from the Pt capsules by means of the micro-holes, and which migrated from the cold or hot part toward another location in the Au tube. Very few particles were found in the niches. Consequently, only TEM-EDS analyses were possible on these samples.

In the hot parts. The particles of the experiments 6m-ip300 (circles) and 10m-ip300 (stars) in the hot parts on the Au tube walls (6m-ip300/300Au and 10m-ip300/300Au, empty symbols) were compared to those inside the Pt capsules (6m-ip300/300Pt and 10m-ip300/300Pt, filled symbols) (Figure 7). The particles were at the same temperature (300ºC) but the crystal chemistry was very different. The particles on the Au tube walls were further away from the starting smectite, displaying slightly smaller I.C. values and smaller Si contents (Figure 7a). The Na contents were very small whereas the Ca contents remained constant (Figure 7e). The total Al contents decreased drastically from 2.17 to 0.43 (Figure 7b). The Fe contents increased (to 3.1 in sample 6m-ip300/300Au) (Figure 7c). The Mg contents were variable, ranging between 0.17 and 0.87, but all the points were on the line of Fe-Mg substitution at constant Fe+Mg in the Fe *vs.* Mg diagram (Figure 7c). The Fe/(Fe+Mg) ratio for sample 6mip300/300Au was greater (Figure 7d). As previously observed in sample 10m-ip80/300Pt (Figure 5), unrealistic negative values for ^{VI}Al were calculated but the structural formulae calculated on the basis of $O_{10}(OH)_8$ instead of $O_{10}(OH)_2$ became coherent again. Finally, the rate of transformation of the particles on the Au tube walls was greater after 6 months (6mip300/300Au) than after 10 months (10m-ip300/300Au), which probably resulted from the different thermal gradients as the cold part in experiment 6m-ip300 was at 100ºC instead of 80ºC. The greater temperature range may have enhanced reactions.

Along the gold tube walls (intermediary sections). The crystal chemistry of the clay particles on the Au tube walls of the experiment 6m-ip100 (triangles in Figure 8) were compared to those inside the Pt capsules (circles in Figure 8). The extent of modifications was greater for particles on the Au tube walls than in the Pt capsules, even at the lowest temperature. The nature of the evolution was also very different. At 145ºC (white triangles), the clay particles were depleted in Si at a constant I.C. (Figure 8a), enriched in Fe, but Mg was absent (Figure 8c,d). The Al content was about constant (Figure 8b). The particles were also enriched in Ca but totally depleted in Na (Figure 8e). At 220ºC (black triangles), the Si content was very small at a constant I.C. (Figure 8a), the Al content decreased slightly (Figure 8b), the Fe content was enriched at various Mg contents (Figure 8c,d), and Ca was enriched but Na was totally depleted (Figure 8e). The sample at 180ºC (gray triangles) contained particles that fell into two categories, one near the sample at 145ºC and the other near the sample at 220ºC. Some particles were enriched in Al: these were also depleted in Fe and Mg.

Mass transport clearly occurred along the Au tube. Mg was absent from the samples in the niches, except for some particles at 200ºC, whereas a weak enrichment was observed in the hot part (6m-ip100/300Pt); therefore, Mg probably migrated toward the hottest part of the tube. Ca was absent from the particles inside the Pt capsule in the cold part but was found in all samples at the highest temperature. Except for some particles at 180ºC, Fe enrichment increased with temperature for particles on the Au tube walls. Finally, a chemical discontinuity in sample 6m-ip100/180Au may correspond to a transition in reaction paths at 180ºC.

The differences in experimental conditions between the particles on the Au tube wall and inside the Pt capsules were the L/C ratio and the Fe availability; the clay particles in the Pt capsules were confined to Fe particles whereas those in the Au tube were more dispersed in the fluid. Chemical reactions were, therefore, assumed to be enhanced and modified in the Au tube because of greater particle-fluid exchange and interaction. The particles on the Au tube walls could also have come from precipitation processes, the fluid being enriched in some elements issued from the dissolution of the clay particles inside the Pt capsules.

https://doi.org/10.1346/CCMN.2010.0580506 Published online by Cambridge University Press

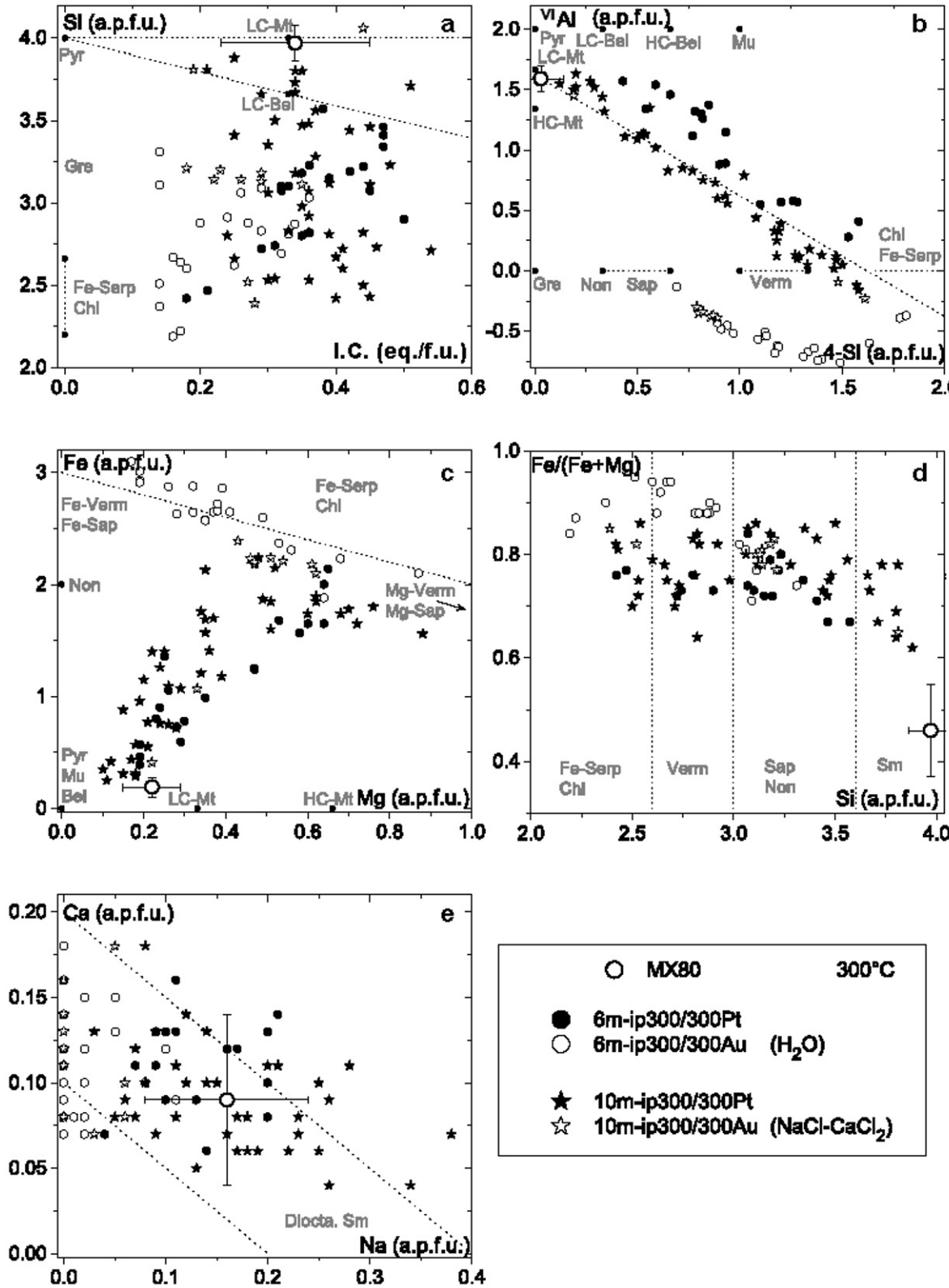

Figure 7. Comparison between the crystal chemistry of the clay phase in the Au tube (Au) and inside the Pt capsule (Pt) in the hot part of experiments 6m-ip300 and 10m-ip300. The Fe plates were located in the hot parts in both experiments. (a) Si *vs.* I.C.; (b) ^{VI}Al *vs.* 4-Si; (c) Fe *vs.* Mg; (d) Fe/(Fe+Mg) *vs.* Si; (e) Ca *vs.* Na. See Figure 5 for symbol legend and axis units.

https://doi.org/10.1346/CCMN.2010.0580506 Published online by Cambridge University Press

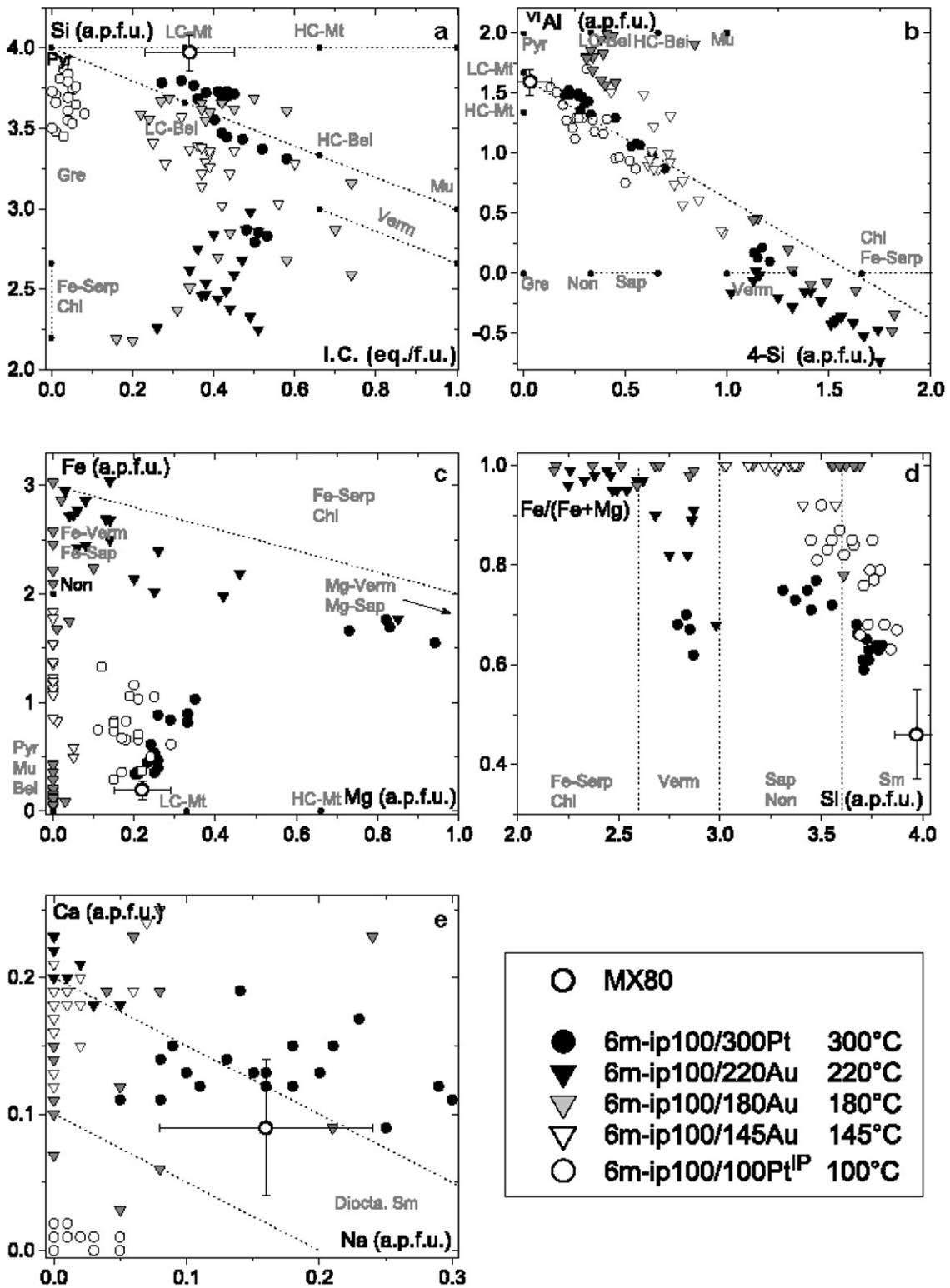

Figure 8. Crystal chemistry of the clay phase on the Au tube walls as a function of temperature (triangles) and compared to the contents of the Pt capsules (circles) of experiment 6mip100. The experiment ran in a pure water medium. The Fe plate was in the cold part. (a) Si *vs.* I.C.; (b) ^{VI}Al *vs.* 4-Si; (c) Fe *vs.* Mg; (d) Fe/(Fe+Mg) *vs.* Si; (e) Ca *vs.* Na. See Figure 5 for symbol legend and axis units.

https://doi.org/10.1346/CCMN.2010.0580506 Published online by Cambridge University Press

Crystallography of the clay fraction (XRD)

Samples inside the platinum capsules. The XRD pattern of the initial MX80 (Figure 9a) displayed the typical diffraction peaks of MX80 with dioctahedral Na-Ca smectite at 12.2 Å and 4.49 Å, a trace of mica at 10.1 Å, quartz at 3.35 Å, cristobalite at 4.05 Å, and feldspars at ~3.22 Å. After 10 months, no metallic Fe was present but magnetite appeared. The signals of quartz and feldspar were less intense. In the hot parts (Figure 9b,c), the 001 peak of smectite at 12.2 Å was significantly modified, with a decrease in intensity and the growth of a 14 Å peak. Albite was formed (peaks at 4.04 Å, 3.21 Å, and 3.17 Å). A large peak at 7.15 Å appeared in the XRD pattern of sample 10m-ip80/300Pt. In the cold parts (Figure 9d,e), the 001 peak of smectite at 12.2 Å was broadened; all other peaks were attributed to magnetite. These results were in good agreement with the TEM-EDS data; the starting, low-charge montmorillonite evolved toward Fe-serpentine and/or chlorite products in the hot parts but few changes were visible in the cold parts.

Sample on the gold tube walls. The XRD pattern of the powder on the Au tube walls of sample 10m-ip80/300Au was virtually the same as those of the samples from the Pt capsules. The 001 peak of smectite shifted toward 14.2 Å (Figure 10). After glycolation, it shifted to 17 Å but a non-swelling part remained at 14.2 Å. This result confirmed the formation of chlorite at 300ºC, as previously observed by Guillaume *et al.* (2003).

Iron redox of the clay particles

The chemical environment and oxidation state of Fe in samples 6m-ip300/300Pt, 6m-ip300/100Pt, 6m-ip100/300Pt, and 6m-ip100/100Pt were measured using TMS (Table 2). Iron was found only in magnetite and the clay structure. Magnetite could result either from the oxidation of the metallic Fe or unreacted initial magnetite. No Fe (oxyhydr)oxides other than magnetite and no metallic Fe were detected, in agreement with XRD data. In the starting montmorillonite, Fe was present as Fe(II) and Fe(III) with an Fe(III)/Fe_{Tot} ratio of 0.55 (Guillaume, 2002; Guillaume *et al.*, 2004). After reaction, Fe was only present as Fe(III) in the samples in the cold parts

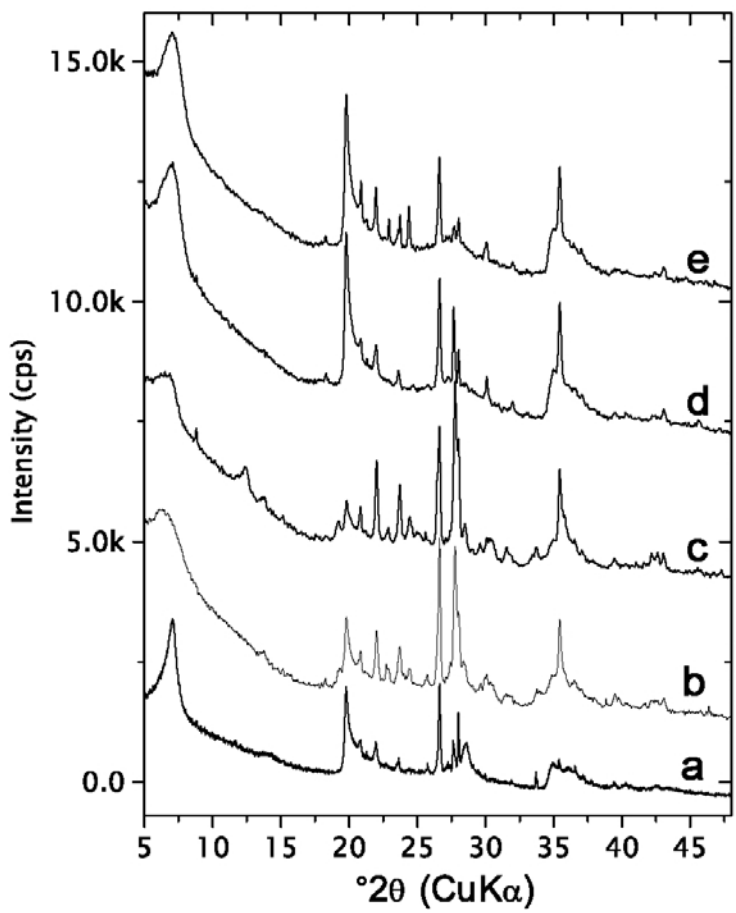

Figure 9. XRD patterns of the initial MX80 bentonite (a); and of the products from experiments 10m-ip300 and 10m-ip80: (b) 10m-ip300/300Pt (with an Fe plate); (c) 10m-ip80/300Pt; (d) 10m-ip300/80Pt; (e) 10m-ip80/80Pt (with an Fe plate).

https://doi.org/10.1346/CCMN.2010.0580506 Published online by Cambridge University Press

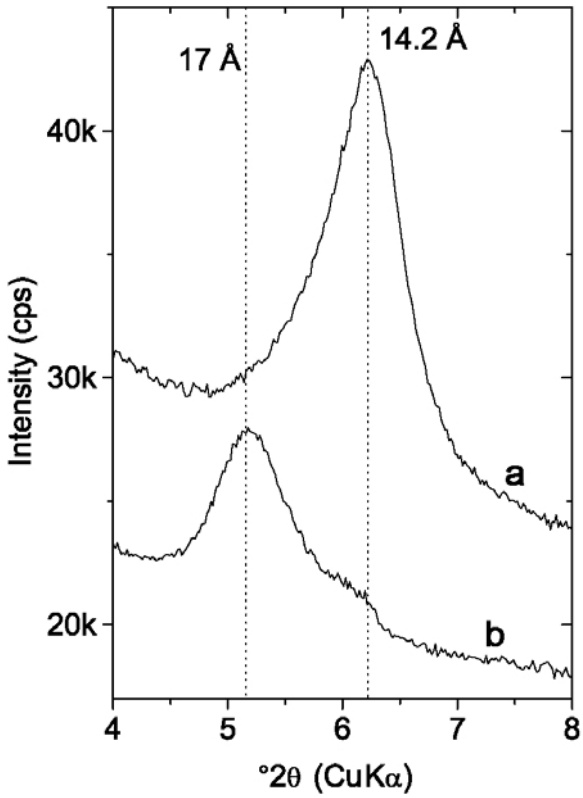

Figure 10. XRD pattern of the particles on the Au tube walls of sample 10m-ip80/300Au: (a) raw powder spectrum; (b) powder spectrum after addition of one droplet of ethylene glycol to the powder.

(6m-ip300/100Pt, 6m-ip100/100Pt), whereas the samples in the hot parts (6m-ip300/300Pt and 6m-ip100/300Pt) contained both Fe(III) and Fe(II). The sample with the largest Fe(II) content was sample 6mip300/300Pt, at 300ºC with an Fe plate. The sample with the greatest amount of magnetite was sample 6m-ip300/100Pt at 100ºC without an Fe plate.

A small amount of magnetite and a small $Fe(III)/Fe_{tot}$ ratio indicate a reductive medium. On the contrary, a greater magnetite content and $Fe(III)/Fe_{tot}$ ratio correspond to a more oxidative medium. The most oxidized sample was 6m-ip300/100Pt, in the cold part and without an Fe plate, and the most reduced one was 6m-ip300/300Pt, in the hot part with an Fe plate. So more reductive conditions were found at elevated temperature with more Fe. Greater temperatures probably resulted in the greatest rate of corrosion of Fe, meaning that there was more H_2 and more-reducing conditions.

Crystal-chemical data from TEM-EDS and the $Fe(III)/Fe_{tot}$ ratio from TMS of experiments 6mip300 and 6m-ip100 are illustrated in the $Fe(III)+{}^{VI}Al$ *vs.* Fe(II)+Mg diagram (Figure 11). The samples in the cold parts remained in the dioctahedral domain of smectite, except the $Fe(III)+{}^{VI}Al$ ratios were larger than in the starting material, due to the increase of the $Fe(III)/Fe_{Tot}$ ratio to a value of ~1. The samples in the hot parts reached values nearer to the trioctahedral domain as a result of the loss of ^{VI}Al and the increase of both the Mg and Fe(II) contents (Figure 5). The shift toward the trioctahedral domain was greater for sample 6m-ip300/300Pt, which presented the lowest $Fe(III)/Fe_{Tot}$ ratio.

Table 2. Mössbauer hyperfine parameters at 78 K of samples 6m-ip300/300Pt, 6m-ip300/100Pt, 6m-ip100/300Pt, and 6m-ip100/100Pt.

Sample	Site	δ (mm s^{-1})	Δ or 2ε (mm s^{-1})	H (kOe)	Relative area (%)	$Fe(III)^c/Fe_{tot}{}^c$
6m-ip300/300Pt^{IP}	$Fe(III)^c$	0.38	0.95	–	29.5	0.41
	$Fe(II)^c$	1.13	2.51	–	41.7	
	Sextet 1	0.16	0	485	13.8	
	Sextet 2	0.7	0	454	15.1	
6m-ip300/100Pt	$Fe(III)^c$	0.37	0.68	–	84.3	1
	Sextet 1	0.36	0	490	5.8	
	Sextet 2	0.65	0	454	10.0	
6m-ip100/300Pt	$Fe(III)^c$	0.37	0.69	–	57.2	1
	Sextet 1	0.3	0	490	17.1	
	Sextet 2	0.67	0	454	25.7	
6m-ip100/100Pt^{IP}	$Fe(III)^c$	0.42	0.97	–	56.2	0.76
	$Fe(II)^c$	1.09	2.68	–	18.1	
	Sextet 1	0.27	0.10	484	14.1	
	Sextet 2	0.75	0.05	458	11.6	

^{c}: Fe in a clay phase; ^{IP}: presence of an iron plate in the platinum capsule.
δ: center shift; Δ or 2ε: quadrupole splitting; H: hyperfine splitting. Sextets are relative to magnetite.

https://doi.org/10.1346/CCMN.2010.0580506 Published online by Cambridge University Press

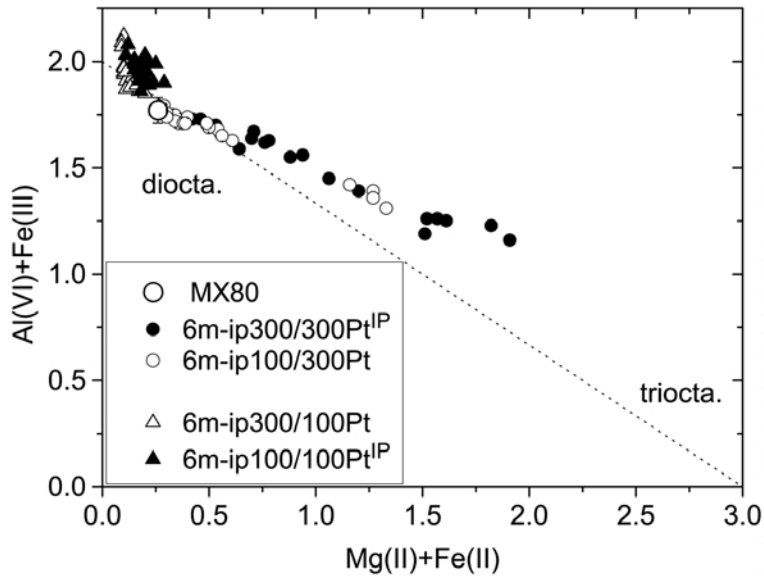

Figure 11. Evolution of the Fe oxidation state of the clay particles in samples 6m-ip300/300Pt, 6m-ip100/300Pt, 6mip300/100Pt, and 6m-ip100/100Pt. ^{VI}Al, Mg, and total Fe from TEM-EDS; Fe(III) to Fe(II) ratio from TMS. IP: position of the Fe plate; circles: hot parts; triangles: cold part; filled symbols: presence of an Fe plate; empty symbol: without Fe plate.

These results agreed perfectly with those of Guillaume *et al.* (2004), who observed a transition toward the trioctahedral domain of smectite by enrichment in Fe(II) at 300ºC and only Fe(III) at 80ºC, in agreement with the Eh/pH measurements in the solutions.

CONCLUSIONS

In the Pt capsules, reaction paths at elevated temperatures were similar to those described previously in batch experiments at constant temperature; in the presence of Fe oxides and metallic Fe, the initial dioctahedral, low-charge smectite was destabilized toward trioctahedral products, enriched in Fe and Mg. The most evolved products were probably chlorite at 300ºC. At lower temperature, the transformation rate was lower but the clay minerals were enriched in Fe, as Fe-serpentine or chlorite. At the same time, mica dissolved, Fe oxidized to magnetite, and newly formed phases appeared (quartz, amorphous silica, and albite). Mass transport processes were observed as a consequence of the thermal gradient, which affected Mg, in particular. Compared to batch experiments, the reactions at the lowest temperatures were more sensitive to the thermal gradient than at 300ºC. Reactivity was probably enhanced at the lowest temperature by faster reactions at the hot end of the Au tube. The redox conditions also appeared to be different in the hot and cold parts, with or without an Fe plate. The comparison of the nature of the products between the samples inside the Pt capsules and on the Au tube walls also highlights the strong influence of the liquid-to-clay ratio on the rate and paths of the reactions.

ACKNOWLEDGMENTS

This research was supported financially by ANDRA - Agence Nationale pour la Gestion des Déchets Radioactifs (French National Agency for the Management of Radioactive Wastes).

The authors thank J. Ghanbaja (SCMEM, Université Henri Poincaré, Vandœuvre-lès-Nancy, France) for the TEM-EDS analyses and M. Abdelmoula (LCPME, Université Henri Poincaré, Villers-lès-Nancy, France) for TMS measurements and interpretation.

REFERENCES

Baldeyrou, A., Vidal, O., and Fritz, B. (2003) Étude expérimentale des transformations de phase dans un gradient thermique: application au granite de Soultz-sous-Forêts, France. Experimental study of phase transformations in a thermal gradient: application to the Soultz-sous-Forêts granite (France). *Comptes Rendus Geosciences*, **335**, 371–380.

Bildstein, O., Trotignon, L., Perronnet, M., and Jullien, M. (2006) Modelling iron-clay interactions in deep geological disposal conditions. *Physics and Chemistry of the Earth, Parts A/B/C*, **31**, 618–625.

Caillère, S., Hénin, S., and Rautureau, M. (1982) *Minéralogie des Argiles. Structure et Propriétés Physico-Chimiques*. Masson, Paris, 184 pp.

Carlson, L., Karnland, O., Oversby, V.M., Rance, A.P., Smart, N.R., Snellman, M., Vähänen, M., and Werme, L.O. (2007) Experimental studies of the interactions between anaerobically corroding iron and bentonite. *Physics and Chemistry of the Earth, Parts A/B/C*, **32**, 334–345.

Charpentier, D., Devineau, K., Mosser-Ruck, R., Cathelineau, M., and Villiéras, F. (2006) Bentonite-iron interactions under alkaline condition: An experimental approach. *Applied Clay Science*, **32**, 1–13.

Chipman, J. (1926) The Soret effect. *Journal of the American Chemical Society*, **48**, 2577–2589.

de Combarieu, G., Barboux, P. and Minet, Y. (2007) Iron corrosion in Callovo-Oxfordian argilite: From experiments

https://doi.org/10.1346/CCMN.2010.0580506 Published online by Cambridge University Press

to thermodynamic/kinetic modelling. *Physics and Chemistry of the Earth*, **32**, 346–358.

Goffé, B., Murphy, W.M., and Lagache, M. (1987) Experimental transport of Si, Al and Mg in hydrothermal solutions: an application to vein mineralization during high-pressure, low-temperature metamorphism in the French Alps. *Contributions to Mineralogy and Petrology*, **97**, 438–450.

Guillaume, D. (2002) Étude expérimentale du système fer-smectite en présence de solution à 80ºC et 300ºC. PhD thesis, Université Henri Poincaré, Nancy, France, 216 pp.

Guillaume, D., Neaman, A., Cathelineau, M., Mosser-Ruck, R., Peiffert, C., Abdelmoula, M., Dubessy, J., Villiéras, F., Baronnet, A., and Michau, N. (2003) Experimental synthesis of chlorite from smectite at 300ºC in the presence of metallic Fe. *Clay Minerals*, **38**, 281–302.

Guillaume, D., Neaman, A., Cathelineau, M., Mosser-Ruck, R., Peiffert, C., Abdelmoula, M., Dubessy, J., Villiéras, F., and Michau, N. (2004) Experimental study of the transformation of smectite at 80 and 300ºC in the presence of Fe oxides. *Clay Minerals*, **39**, 17–34.

Kostov, I. (1968) *Mineralogy*. Oliver and Boyd, Edinburgh and London, 587 pp.

Lantenois, S., Lanson, B., Muller, F., Bauer, A., Jullien, M., and Plançon, A. (2005) Experimental study of smectite interaction with metal Fe at low temperature: 1. Smectite destabilization. *Clays and Clay Minerals*, **53**, 597–612.

Madsen, F.T. (1998) Clay mineralogical investigations related to nuclear waste disposal. *Clay Minerals*, **33**, 109–129.

Martin, F.A., Bataillon, C., and Schlegel, M.L. (2008) Corrosion of iron and low alloyed steel within a water saturated brick of clay under anaerobic deep geological disposal conditions: An integrated experiment. *Journal of Nuclear Materials*, **379**, 80–90.

Martín, M., Cuevas, J., and Leguey, S. (2000) Diffusion of soluble salts under a temperature gradient after the hydration of compacted bentonite. *Applied Clay Science*, **17**, 55–70.

Neaman, A., Guillaume, D., Pelletier, M., and Villiéras, F. (2003) The evolution of textural properties of Na/Ca-bentonite following hydrothermal treatment at 80 and 300ºC in the presence of Fe and/or Fe oxides. *Clay Minerals*, **38**, 213–223.

Paszkuta, M., Rosanne, M., and Adler, P.M. (2006) Transport coefficients of saturated compact clays. *Comptes Rendus Geosciences*, **338**, 908–916.

Perronnet, M., Villiéras, F., Jullien, M., Razafitianamaharavo, A., Raynal, J., and Bonnin, D. (2007) Towards a link between the energetic heterogeneities of the edge faces of smectites and their stability in the context of metallic corrosion. *Geochimica et Cosmochimica Acta*, **71**, 1463–1479.

Perronnet, M., Jullien, M., Villiéras, F., Raynal, J., Bonnin, D., and Bruno, G. (2008) Evidence of a critical content in Fe(0) on FoCa7 bentonite reactivity at 80ºC. *Applied Clay Science*, **38**, 187–202.

Poinssot, C., Goffé, B., Magonthier, M.-C. and Toulhoat, P. (1996) Hydrothermal alteration of a simulated nuclear waste glass; effects of a thermal gradient and of a chemical barrier. *European Journal of Mineralogy*, **8**, 533–548.

Poinssot, C., Jullien, M., and Pozo, C. (1997) Du gradient thermique comme moteur de la migration et des transformations minéralogiques. Pp. 196–203 in: *Rapport Scientifique 1997*, CEA, Saclay, France.

Poinssot, C., Toulhoat, P., and Goffé, B. (1998) Chemical interaction between a simulated nuclear waste glass and different backfill materials under a thermal gradient. *Applied Geochemistry*, **13**, 715–734.

Robert, C. and Goffé, B. (1993) Zeolitization of basalts in subaqueous freshwater settings: Field observations and experimental study. *Geochimica et Cosmochimica Acta*, **57**, 3597–3612.

Rosanne, M., Paszkuta, M., Tevissen, E., and Adler, P.M. (2003) Thermodiffusion in compact clays. *Journal of Colloid and Interface Science*, **267**, 194–203.

Rosanne, M., Paszkuta, M., and Adler, P.M. (2006) Thermodiffusional transport of electrolytes in compact clays. *Journal of Colloid and Interface Science*, **299**, 797–805.

Rousset, D., Guillaume, D., Cathelineau, M., Dubessy, J., Mosser-Ruck, R., Rouiller, A., and Michau, N. (2006) Experimental reactivity of bentonite under linear thermal gradient. Bridging Clay: 43rd Annual Meeting of the CMS & 4ème Colloque du GFA, June 3–7, Oléron, France.

Sauzéat, E., Guillaume, D., Villiéras, F., Dubessy, J., François, M., Pfeiffert, C., Pelletier, M., Mosser-Ruck, R., Barrès, O., Yvon, J., and Cathelineau, M. (2001) *Caractérisation minéralogique, cristallochimique et texturale de l'argilite MX80*. Paris.

Savage, D., Watson, C., Benbow, S., and Wilson, J. (2010) Modelling iron-bentonite interactions. *Applied Clay Science*, **47**, 91–98.

Schlegel, M.L., Bataillon, C., Benhamida, K., Blanc, C., Menut, D., and Lacour, J.-L. (2008) Metal corrosion and argillite transformation at the water-saturated, high-temperature iron-clay interface: A microscopic-scale study. *Applied Geochemistry*, **23**, 2619–2633.

Trouiller, A. (2006) Le Callovo-Oxfordien du bassin de Paris: du contexte géologique à la modélisation de ses propriétés. *Comptes Rendus Geosciences*, **338**, 815–823.

Vidal, O. (1997) Experimental study of the thermal stability of pyrophyllite, paragonite, and clays in a thermal gradient. *European Journal of Mineralogy*, **9**, 123–140.

Vidal, O. and Durin, L. (1999) Aluminium mass transfer and diffusion in water at 400–550ºC, 2 kbar in the K_2O–Al_2O_3–SiO_2–H_2O system driven by a thermal gradient or by a variation of temperature with time. *Mineralogical Magazine*, **63**, 633–647.

Wilson, J., Cressey, G., Cressey, B., Cuadros, J., Ragnarsdottir, K.V., Savage, D., and Shibata, M. (2006a) The effect of iron on montmorillonite stability. (II) Experimental investigation. *Geochimica et Cosmochimica Acta*, **70**, 323–336.

Wilson, J., Savage, D., Cuadros, J., Shibata, M., and Ragnarsdottir, K.V. (2006b) The effect of iron on montmorillonite stability. (I) Background and thermodynamic considerations. *Geochimica et Cosmochimica Acta*, **70**, 306–322.

(*Received 23 February 2010; revised 3 October 2010; Ms. 412; A.E. P. Komadel*)